

Mathematical model of thermal shields for long-term stability optical resonators

Josep Sanjuan,¹ Norman Gürlebeck² and Claus Braxmaier^{1,2}

¹German Aerospace Center (DLR), Robert-Hooke-Str. 7, Bremen 28359, Germany

²Center of Applied Space Technology and Microgravity (ZARM), University of Bremen, Am Fallturm 1, 28359 Bremen, Germany

[*jose.sanjuan@dlr.de](mailto:jose.sanjuan@dlr.de)

Abstract: Modern experiments aiming at tests of fundamental physics, like measuring gravitational waves or testing Lorentz Invariance with unprecedented accuracy, require thermal environments that are highly stable over long times. To achieve such a stability, the experiment including typically an optical resonator is nested in a thermal enclosure, which passively attenuates external temperature fluctuations to acceptable levels. These thermal shields are usually designed using tedious numerical simulations or with simple analytical models. In this paper, we propose an accurate analytical method to estimate the performance of passive thermal shields in the frequency domain, which allows for fast evaluation and optimization. The model analysis has also unveiled interesting properties of the shields, such as dips in the transfer function for some frequencies under certain combinations of materials and geometries. We validate the results by comparing them to numerical simulations performed with commercial software based on finite element methods.

© 2021 Optical Society of America

OCIS codes: (120.2230) Fabry-Perot; (120.6810) Thermal effects; (120.3930) Metrological instrumentation.

References and links

1. P. Amaro-Seoane, S. Aoudia, S. Babak, P. Binétruy, E. Berti, A. Bohé, C. Caprini, M. Colpi, N. J. Cornish, K. Danzmann, J.-F. Dufaux, J. Gair, O. Jennrich, P. Jetzer, A. Klein, R. N. Lang, A. Lobo, T. Littenberg, S. T. McWilliams, G. Nelemans, A. Petiteau, E. K. Porter, B. F. Schutz, A. Sesana, R. Stebbins, T. Sumner, M. Vallisneri, S. Vitale, M. Volonteri, and H. Ward, “Low-frequency gravitational-wave science with eLISA/NGO,” *Class. Quantum Grav.* **29**(12), 124016 (2012).
2. O. Jennrich, “LISA technology and instrumentation,” *Class. Quantum Grav.* **26**(15), 153001 (2009).
3. G. Mueller, P. McNamara, I. Thorpe, and J. Camp, “Laser frequency stabilization for LISA,” NASA GSFC Tech. Report 20060012084 (2005).
4. B. S. Sheard, G. Heinzel, K. Danzmann, D. A. Shaddock, W. M. Klipstein, and W. M. Folkner, “Intersatellite laser ranging instrument for the GRACE follow-on mission,” *J. Geodesy* **86**(12), 1083-1095 (2012).
5. W. Folkner, G. de Vine, W. Klipstein, K. McKenzie, D. Shaddock, R. Spero, R. Thompson, D. Wuchenich, N. Yu, M. Stephens, J. Leitch, M. Davis, J. de Cino, C. Pace, and R. Pierce, “Laser frequency stabilization for GRACE-II,” Jet Propulsion Laboratory, California Institute of Technology Tech. Report (2010).
6. C. Braxmaier, H. Müller, O. Pradl, J. Mlynek, A. Peters, and S. Schiller, “Tests of relativity using a cryogenic optical resonator,” *Phys. Rev. Lett.* **88**, 010401 (2001).
7. M. E. Tobar, P. Wolf, S. Bize, G. Santarelli, and V. Flambaum, “Testing local Lorentz and position invariance and variation of fundamental constants by searching the derivative of the comparison frequency between a cryogenic sapphire oscillator and hydrogen maser,” *Phys. Rev. D* **81**, 022003 (2010).
8. H. Müller, S. Herrmann, C. Braxmaier, S. Schiller, and A. Peters, “Modern Michelson-Morley experiment using cryogenic optical resonators,” *Phys. Rev. Lett.* **91**, 020401 (2003).

9. S. Herrmann, A. Senger, K. Möhle, M. Nagel, E. V. Kovalchuk, and A. and Peters, “Rotating optical cavity experiment testing Lorentz invariance at the 10^{-17} level,” *Phys. Rev. D* **80**, 105011 (2009).
10. C. Lämmerzahl, H. Dittus, A. Peters, and S. Schiller, “OPTIS: a satellite-based test of special and general relativity,” *Class. Quantum Grav.* **18**(13), 2499 (2001).
11. J. A. Lipa, S. Buchman, S. Saraf, J. Zhou, A. Alfauwaz, J. Conklin, G. D. Cutler, and R. L. Byer, “Prospects for an advanced Kennedy-Thorndike experiment in low Earth orbit,” *ArXiv e-prints* 1203.3914 gr-qc (2012).
12. A. Milke, D. N. Aguilera, N. Gürlebeck, T. Schuldt, S. Herrmann, K. Döringshoff, R. Spannagel, C. Lämmerzahl, A. Peters, B. Biering, H. Dittus, and C. Braxmaier, “A space-based optical Kennedy-Thorndike experiment testing special relativity,” *European Frequency and Time Forum International Frequency Control Symposium (EFTF/IFC)*, 912-914 (2013).
13. A. Alan Kostelecký and N. Russell, “Data tables for Lorentz and *CPT* violation,” *Rev. Mod. Phys.* **83**, 11-31 (2011).
14. J. D. Tasson, “What do we know about Lorentz invariance?,” *Reports on Progress in Physics* **77**(6), 062001 (2014).
15. S. A. Webster, M. Oxborrow, S. Pugla, J. Millo, and P. Gill, “Thermal-noise-limited optical cavity,” *Phys. Rev. A* **77**(3), 033847 (2008).
16. B. Argençe, E. Prevost, T. Lévêque, R. Le Goff, S. Bize, P. Lemonde, and G. Santarelli, “Prototype of an ultra-stable optical cavity for space applications,” *Opt. Express* **20**(23), 25409–25420 (2012).
17. S. Amairi, T. Legero, T. Kessler, U. Sterr, J. Wbbena, O. Mandel, and P. Schmidt, “Reducing the effect of thermal noise in optical cavities,” *Appl. Phys. B* **113**(2), 233-242 (2013).
18. Q-F. Chen, A. Nevsky, M. Cardace, S. Schiller, T. Legero, S. Häfner, A. Uhde, and U. Sterr, “A compact, robust, and transportable ultra-stable laser with a fractional frequency instability of 1×10^{-15} ,” *Rev. Sci. Instrum.* **85**(11) (2014).
19. M. J. Edwards, E. H. Bullock, and D. E. Morton, “Improved precision of absolute thermal-expansion measurements for ULE glass,” *Advanced Materials for Optical and Precision Structures*, Society of Photo-Optical Instrumentation Engineers (SPIE) Conference Series **2857**, 58-63 (1996).
20. K. P. Birch and P. T. Wilton, “Thermal expansion data for Zerodur from 247 to 373 K,” *Appl. Opt.* **27**(14), 2813–2815 (1988).
21. J. Alnis, A. Matveev, N. Kolachevsky, T. Udem, and T. W. Hänsch, “Subhertz linewidth diode lasers by stabilization to vibrationally and thermally compensated ultralow-expansion glass Fabry-Pérot cavities,” *Phys. Rev. A* **77**(5), 053809 (2008).
22. M. Notcutt, C. T. Taylor, A. G. Mann, and D. G. Blair, “Temperature compensation for cryogenic cavity stabilized lasers,” *J. Phys. D: Appl. Phys.* **28**(9), 1807 (1995).
23. T. Legero, T. Kessler, and U. Sterr, “Tuning the thermal expansion properties of optical reference cavities with fused silica mirrors,” *J. Opt. Soc. Am. B* **27**(5), 914–919 (2010).
24. H. Peabody and S. M. Merkwitz, “Low frequency thermal performance of the LISA sciencecraft,”
25. M. Nofrarias, F. Gibert, N. Karnesis, A. F. García, M. Hewitson, G. Heinzel, and K. Danzmann, “Subtraction of temperature induced phase noise in the LISA frequency band,” *Phys. Rev. D* **87**(10), 102003 (2013). *AIP Conference Proceedings* **873**, 204-209 (2006).
26. T. L. Bergman, A. S. Lavine, F. P. Incropera, and D. P. DeWitt, *Fundamentals of Heat and Mass Transfer* (Wiley, 2011).
27. M. Nofrarias, “Thermal diagnostics in the LISA technology package,” Ph.D Thesis, Universitat de Barcelona (2007).
28. A. Lobo, M. Nofrarias, J. Ramos-Castro, and J. Sanjuan, “On-ground tests of the LISA Pathfinder thermal diagnostics system,” *Class. Quantum Grav.* **23**(17), 5177 (2006).
29. H. S. Carslaw and J. C. Jaeger, *Heat Conduction in Solids* (Oxford Science Publications, 1986).

1. Introduction

The ever increasing accuracy of current and future fundamental physics experiments on ground and in space demands very stable and controlled environments to meliorate spurious effects such as temperature fluctuations. In this paper, we present a method that allows the rapid assessment of the performance of passive thermal shields in the frequency domain. This is done with analytical models instead of time consuming and precision limited numerical simulations. The frequency domain is of special interest since stability requirements are typically given in such domain.

One of the key applications of this method is the design of thermal isolations for optical resonators (ORs), which are used as frequency references in highly sensitive interferometers, in experiments testing fundamental physics, and as optical frequency standards, see e.g. [1–5],

[6–14], and [15–18], respectively. ORs consist of a spacer and two high-reflectivity mirrors. The distance between the mirrors defines the resonance frequency, which is directly linked to the length of the spacer. Consequently, temperature fluctuations result in frequency fluctuations, i.e.,

$$\frac{\delta\nu}{\nu} = \frac{\delta\ell}{\ell} = \alpha\delta T, \quad (1)$$

where ν is the optical frequency, ℓ is the spacer length, α is the spacer coefficient of thermal expansion (CTE) and T is its temperature. Fluctuations of the variables are expressed as δ . The spacers of ORs are made of materials with very low CTEs, e.g. ultra low expansion glass (ULE) or Zerodur with CTEs about 10^{-8} K^{-1} at room temperature [19, 20]. In addition, the ORs are often driven at temperatures close to their CTE zero crossing (or at the CTE minimum) [15, 21]. In case these temperatures cannot be achieved, different techniques have been developed to tune the temperature of the zero crossing [22, 23]. Nevertheless, the accuracy of current optical experiments is already so high that these low CTEs do not suffice and temperature fluctuations need to be strongly attenuated. The damping of temperature fluctuations at frequencies in the milli-Hertz and sub-milli-Hertz regime by several orders of magnitude demands a particularly careful thermal shield design. This low frequency range is crucial in different missions and experiments since the expected science signals are in the same frequency band. This is especially important for the space-based gravitational wave detector eLISA [1] and foreseen missions testing the fundamental principles of general relativity such as the Lorentz Invariance with Michelson-Morley experiments and a Kennedy-Thorndike experiment like STAR (SpaceTime Asymmetry Research [11]), mini-STAR, and BOOST (BOOST Symmetry Test [12]), for earlier Kennedy-Thorndike experiments see, e.g., [6, 7].

The thermal shield design is driven by the required temperature stability of the OR, i.e., the required frequency stability for a given spacer CTE, and the temperature variations at the outer most thermal shield layer. For eLISA the required temperature stability (if a cavity is used for the laser pre-stabilization) is $\mu\text{K Hz}^{-1/2}$ in the mili-Hertz band. The thermal environment in eLISA will be extremely stable [24] and the required attenuation will not be very demanding. However, the main problem is for laboratory-based demonstration experiments [2, 25] where $\mu\text{K Hz}^{-1/2}$ temperature stability in the sub-milli-Hertz range is needed. For the Kennedy Thorndike experiments the allowed temperature fluctuations are typically $\lesssim 0.1 \mu\text{K}$ at the orbital period (~ 90 minutes) and the expected stability in the satellites around 1 K and $\sim 10 \text{ mK}$ can be achieved in the payload by active temperature control. This poses a stringent requirement on the thermal shields: about five orders of magnitude attenuation at $\sim 0.2 \text{ mHz}$. For the Gravity Recovery and Climate Experiment Follow-On (GRACE-FO) interferometer similar figures are required [5]. The thermal shield performance is usually estimated with the help of tedious numerical simulations [16, 24] or with rather simplified analytical models. However, a method to estimate its transfer function yielding results close to the numerical simulations is to our best knowledge still lacking. In this paper, we provide such a tool, using thermal shields for optical resonators as an example.

The paper is organized as follows: First the general mathematical model is introduced, which is applied to the cases of spherical and cylindrically shaped shields in Sec. 3. These results are compared with numerical simulations based on finite element methods (FEM) in Sec. 4. Sec. 5 summarizes our conclusions. Supplementary models and mathematical details are provided in the appendix.

2. Mathematical model of the thermal shields

The basic assumption of the thermal shields' mathematical model is that heat is transferred only by radiation and conduction. In Sec. 2.1, the analytical transfer function of the thermal shields

is derived, when the latter is negligible. In Sec. 2.2, the conductive links between the shields are included in the model, too.

2.1. Radiative heat transfer

The radiative heat transfer between two gray bodies (from body i to body j) is defined as [26]:

$$\dot{q}_j(t) = \frac{\sigma A_j [T_i^4(t) - T_j^4(t)]}{\beta_{ij}}, \quad (2)$$

where σ is the Stefan-Boltzmann constant ($= 5.67 \times 10^{-8} \text{ W m}^{-2} \text{ K}^{-4}$), A_j is the area, T_j is the temperature in Kelvin of the respective layers and β_{ij} is a term including the view factors and emissivities, ε —see Sec. 3. The temperature change of the layer j due to the heat exchange given by Eq. (2) is

$$\dot{q}_j(t) = m_j c_j \dot{T}_j(t), \quad (3)$$

where m_j and c_j are the mass and the specific heat of the layer j , respectively. We assume that the thermal shields have high thermal conductivity and are relatively thin. Consequently, the temperature distribution in the shields homogenizes rapidly even in the cases, where point heat sources are present —see Sec. 3. Hence, we do not consider a spatial temperature distribution. Combining Eqs. (2) and (3) results in the differential equation

$$\frac{4\sigma A_j T_0^3}{\beta_{ij}} [T_i(t) - T_j(t)] = m_j c_j \dot{T}_j(t) \quad (4)$$

that has been linearized in order to find an analytical solution. T_0 is the average temperature of the bodies. Typically, temperature changes during the experiments are small compared to T_0 and, thus, the linearization is justified.

The transfer function of the thermal shield (from layer i to j) is obtained after applying the Fourier transform to Eq. (4) and taking the ratio between both temperatures:

$$\tilde{H}_{ij}(\omega) = \frac{\tilde{T}_j(\omega)}{\tilde{T}_i(\omega)} = \frac{1}{1 + \frac{m_j c_j \beta_{ij}}{4\sigma A_j T_0^3} i\omega}, \quad (5)$$

which corresponds to a first-order low-pass filter with a cut-off angular frequency of

$$\omega_c = \frac{4\sigma A_j T_0^3}{m_j c_j \beta_{ij}}. \quad (6)$$

Analogously to the electrical case, the cut-off angular frequency is split in a thermal resistance (in units of K W^{-1}) and a thermal capacitance (in units of J K^{-1}):

$$\theta_{ij} = \frac{\beta_{ij}}{4\sigma A_j T_0^3}, \quad (7)$$

$$C_j = m_j c_j \quad (8)$$

and the product is the time constant of the system, $\tau_{ij} = \theta_{ij} C_j = \omega_c^{-1}$.

Once the transfer function of one shield (formed by 2 layers) has been determined the behavior of N concentric thermal shields ($N + 1$ layers) can be calculated. In order to obtain a compact expression, it is assumed that all the layers are exactly the same (in material and in

size), i.e., they all have the same time constant $\tau_{ij} = \tau$. The validity of this assumption is discussed in Sec. 3, where we show that it holds for thin layers that are sufficiently close to each other. In Appendix A, the transfer function for N layers is derived and the result is

$$\begin{aligned}\tilde{H}(\omega) &= \frac{1}{1 + \sum_{k=1}^N \frac{1}{(2k)!} \frac{(N+k)!}{(N-k)!} (i\omega\tau)^k} \\ &= \left(1 + \frac{1}{4}i\omega\tau\right)^{1/2} \sec \left[(2N+1) \csc^{-1} \left(\frac{1+i}{\sqrt{\omega\tau/2}} \right) \right].\end{aligned}\quad (9)$$

This is depicted in Fig. 1 for different N . The left panel shows, how the layers interact with each other causing some of the poles of the transfer function, cf. Eq. (9), of the system to appear at lower frequencies than the poles of each individual layer. For this reason, the system exhibits a stronger temperature damping at frequencies around the cut-off angular frequency than if the layers are assumed uncoupled, i.e.,

$$\tilde{H}(\omega) = (1 + i\omega\tau)^{-N}. \quad (10)$$

However, for $\omega \gtrsim 10\omega_c$ the response of both systems (coupled or uncoupled) is the same and Eq. (10) can be used instead of Eq. (9).

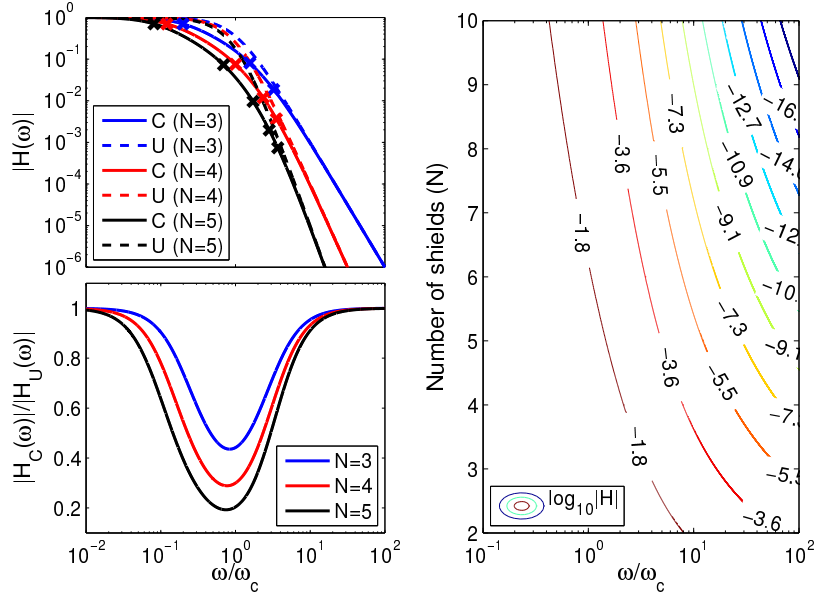


Fig. 1. Left: transfer functions using the coupled case Eq. (9) (solid lines) and the uncoupled case Eq. (10) (dashed lines) for $N = 3, 4$ and 5 . The cut-off angular frequency of each layer is ω_c (cf. Eq. 6). Notice that some of the poles of the exact solution (cross marks) are at lower frequencies than ω_c (C: coupled filters. U: uncoupled filters), which improves the damping for frequencies around ω_c . For $\omega \gtrsim 10\omega_c$ the results are the same. The bottom plot shows the ratio between the coupled and uncoupled solutions. Right: $|\tilde{H}(\omega)|$ as a function of the frequency and the number of layers (in logarithmic scale).

In order to calculate the insulator transfer function, cf. Appendix A, the cut-off angular frequency needs to be well known to avoid errors in $|\tilde{H}(\omega)|$. The errors in the cut-off frequency are due to the assumption that all the time constants of the shields, τ , are the same. The ratio between the transfer function considering a -10% relative error in ω_c and the actual transfer function is shown in Fig. 2. The errors only become significant when large number of layers are used and for $\omega \gg \omega_c$. This will be used in Sec. 3 to assess the validity of the assumption that $\tau_{ij} = \tau$.

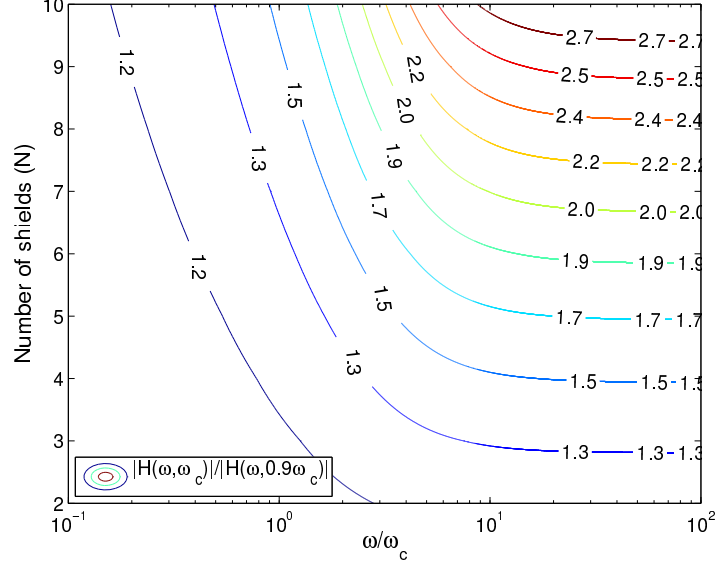


Fig. 2. Ratio between $|H(\omega, \omega_c)|$ and $|H(\omega, 0.9\omega_c)|$ as a function of N and angular frequency. The relative error of the cut-off angular frequency is -10% . The errors in the transfer function are tolerable even for large N if the relative error in ω_c is kept smaller than -10% .

For completeness, we present here the transfer function in the case when the OR is included. The OR acts as an extra low-pass filter. However, its thermal resistance, θ_{OR} , and thermal capacitance, C_{OR} , can be, in general, different from the thermal shield one, i.e., $\tau \neq \tau_{\text{OR}}$. The transfer function is —see Appendix A for details,

$$\tilde{H}(\omega) = \left[1 + \frac{\tau_{\text{OR}}}{\tau} (i\omega\tau)^{N+1} + \sum_{k=1}^N \left[\frac{1}{(2k-1)!} \frac{(N+k-1)!}{(N-k)!} \frac{C_{\text{OR}}}{C} + \frac{1}{(2k-2)!} \frac{(N+k-1)!}{(N-k+1)!} \frac{\tau_{\text{OR}}}{\tau} + \frac{1}{(2k)!} \frac{(N+k)!}{(N-k)!} \right] (i\omega\tau)^k \right]^{-1}, \quad (11)$$

where $\tau_{\text{OR}} = \theta_{\text{OR}} C_{\text{OR}}$. If $\tau_{\text{OR}} \ll \tau$ and $C_{\text{OR}} \ll C$, Eq. (9) is recovered and the effect of the resonator is negligible. Here N is the number of shields without including the resonator. However, in some cases $C_{\text{OR}} \geq C$ since optical resonators are typically bulky bodies made of Zerodur or ULE. The thermal resistance (between the last layer of the thermal shield and the resonator) and thermal capacitance of the resonator are:

$$\theta_{N\text{OR}} \simeq \frac{1}{4\epsilon_N \sigma A_{\text{OR}} T_0^3}, \quad (12)$$

$$C_{\text{OR}} = m_{\text{OR}} c_{\text{OR}}, \quad (13)$$

where it is important to notice that θ_{NOR} does not depend on the resonator's emissivity (assuming $\epsilon_N \ll \epsilon_{\text{OR}}$ and that $r_{\text{OR}} \simeq r_N$, where r_{OR} is a representative radius of the optical resonator), ϵ_{OR} , and for this reason it will usually be similar to θ . If such condition is met and the thermal capacitance of the shield and the resonator are also similar, Eq. (9) with an extra layer can be used instead of Eq. (11).

2.2. Conductive heat transfer

Thermal shield layers need, of course, mechanical supports between them. In this section, the effect of such a support structure on the performance of the thermal shields (2 layers) is analyzed. The supports or thermal links are supposed to have a very low thermal conductivity and, therefore, the lumped model approximation is not adequate. It is not guaranteed that the temperature is uniform along the supports [26–28]. Consequently, the spatial gradient term of the Fourier heat transfer equation needs to be included. In this case, the transfer function of a shield is —see Appendix B for details:

$$\tilde{H}(\omega) = \frac{\sinh \ell q_s + q_s \theta \kappa_s A_s}{(1 + i\omega\tau) \sinh \ell q_s + q_s \theta \kappa_s A_s \cosh \ell q_s} \quad (14)$$

with

$$q_s^2 \equiv \frac{\rho_s c_s}{\kappa_s} i\omega, \quad (15)$$

where κ_s , c_s , ρ_s , A_s and ℓ are the conductivity, the specific heat, the density, the cross section and the length of the supports. Note that the supports are assumed to have the same length and the cross-section is the sum of all of them. For the derivation of the transfer function it has been assumed that no radiative heat transfer occurs between the supports and the thermal shields. Therefore, the model is accurate if the supports are covered with high reflective coating. In Sec. 3.2, a detailed numerical analysis is shown and in Sec. 4 they are compared with FEM simulations.

3. Concentric spheres and concentric cylinders thermal shields

Basically two geometries are used as thermal shields: concentric hollow spheres (or cubes) and concentric hollow cylinders (or rectangular cuboids). The cut-off angular frequency ω_c of a thermal shield defines completely the attenuation of temperature fluctuations if we consider solely radiation. It is given in Eq. (6), where β depends on the geometry of the shields and the emissivity of the material [26]:

$$\beta_{ij} = \frac{1}{\epsilon_j} + \frac{1-\epsilon_i}{\epsilon_i} \left(\frac{r_j}{r_i}\right)^2, \quad \text{for spheres} \quad (16)$$

$$\beta_{ij} = \frac{1}{\epsilon_j} + \frac{1-\epsilon_i}{\epsilon_i} \left(\frac{r_j}{r_i}\right), \quad \text{for (infinitely long) cylinders} \quad (17)$$

where r is the radius. The view factors for finite cylinders, cubes and cuboids are more complicated than the ones given in Eqs. (16) and (17), however, the approximation of cubes to spheres and finite cylinders and cuboids to infinite cylinders yields accurate results —see Sec. 3.2. If the shields are assumed to have approximately equal size ($r_i \approx r_j$) and high reflectivity materials are used ($\epsilon \ll 1$), Eqs. (16) and (17) reduce to $\beta \simeq 2/\epsilon$ and the cut-off angular frequency of a thermal shield is

$$\omega_c = \frac{2\epsilon\sigma T_0^3}{\rho ch}, \quad (18)$$

where h is the thickness of the layers. In Sec. 2.1, we assumed that τ is the same for each shield. Equation (18) shows that this assumption is valid for the aforementioned conditions. However, in Eq. (18) two simplifications have been used: (i) the volume of the hollow sphere (or cylinder) has been approximated to $4\pi r^2 h$ (and similarly for the cylinder) and, (ii) the radius of all layers has been considered the same ($r_i = r_j$). Both of these assumptions cause errors in the calculated cut-off angular frequency. To keep them below 10% —see Fig. 2, the ratio between the inner and outer radii of the layer i has to be $r_{i,\text{in}}/r_{i,\text{out}} \geq 0.9$ for spheres (the layer thickness has to be $h \leq 0.1 r_{\text{out}}$) and $r_{i,\text{in}}/r_{i,\text{out}} \geq 0.8$ for cylinders —see Fig. 3 (top); and the ratio between the radius of two consecutive layers has to be $r_{i+1}/r_i \geq 0.9$ for spheres and $r_{i+1}/r_i \geq 0.8$ for cylinders —see Fig. 3 (bottom). Both conditions, thin layers and small distance between the layers, are usually met when designing and constructing thermal shields.

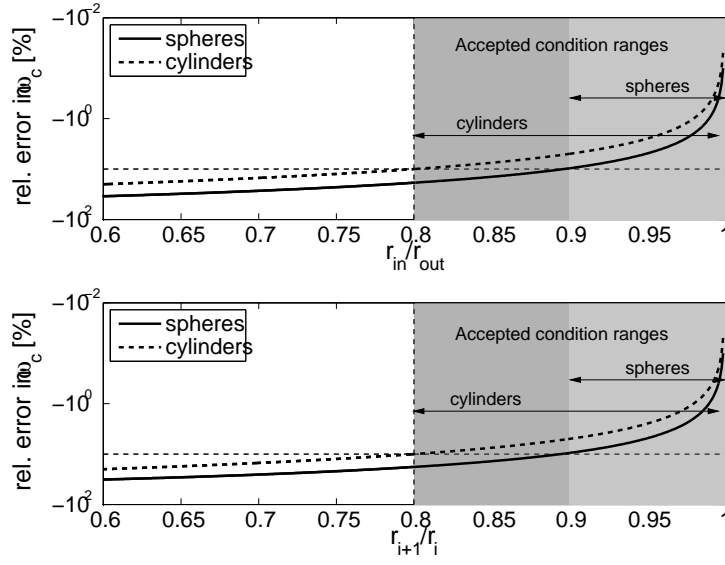


Fig. 3. Top: relative error in ω_c due to approximating the volume of a layer to $4\pi r^2 h$ (or $2\pi r h \ell$ for cylinders). Bottom: relative error in ω_c due to the assumption that the distance between two consecutive layers is zero ($r_i = r_j$) when it is not.

The only assumption in Sec. 2.1, which has not yet been justified, is the one concerning the temperature homogenization of the thermal shields. This matters, when a point-like heat source is present. A homogeneous temperature distribution can be assumed if the time constant of the shield itself is much smaller than the time constant of the radiative heat transfer, i.e., $\tau \gg \tau_{\text{shield}}$. The time constant of the shield is (for the spherical case)

$$\tau_{\text{shield}} = \theta_{\text{shield}} C_{\text{shield}} \sim \frac{2\pi r^2 \rho c}{\kappa} \quad (19)$$

and considering thin layers ($h = 0.1r$):

$$\frac{\tau_{\text{shield}}}{\tau} = \frac{4\pi r}{0.1\kappa} \varepsilon \sigma T_0^3, \quad (20)$$

which is much smaller than one for high reflectivity and high conductivity materials.

3.1. Selection of the material

Given a requirement for the attenuation of temperature fluctuations, the thermal shields can be optimized in either mass or volume. In this section, this is briefly analyzed. For two thermal shields of different materials, A and B, having the same cut-off angular frequency the ratio between the thickness of the shields is (assuming both materials have the same emissivity, which can be easily done by coating the material)

$$\frac{h_B}{h_A} = \frac{\rho_A c_A}{\rho_B c_B} \quad (21)$$

and the mass ratio is

$$\frac{m_A}{m_B} = \frac{r_A^2 c_B}{r_B^2 c_A}. \quad (22)$$

If we want to minimize the volume for a fixed mass of the layer ($m_A = m_B$), a material with a low specific heat should be chosen following Eq. (22). In contrast, if the mass should be minimized for a given radius of the layer ($r_A = r_B$), a material with a high specific heat should be selected.

3.2. Numerical analysis

In this section, a numerical analysis of the equations shown in Sec. 2.1 and Sec. 2.2 is performed. First, Eq. (9) is used to calculate the required number of shields, N , for a given temperature stability requirement. If the attenuation is needed for $\omega \geq 10\omega_c$, the shields can be assumed uncoupled—see Fig. 1, and N is:

$$N \geq \left\lceil -\frac{\log |\tilde{H}_{\text{req}}|}{\log \omega / \omega_c} \right\rceil \text{ for } \omega \gtrsim 10\omega_c, \quad (23)$$

where $\lceil \cdot \rceil$ is the ceiling function. Figure 4 shows the required number of shields for different attenuation levels: from 10^{-7} to 10^{-4} and for two frequencies: $\omega/2\pi=0.1$ mHz and 1 mHz. The shields are assumed to be made of gold coated aluminum ($\epsilon=0.03$) with a thickness of 0.1 mm, 0.5 mm and 1.5 mm, which correspond to cut-off angular frequencies of 60 μ Hz, 12 μ Hz and 4 μ Hz, respectively.

Next, we design the supports between the layers such that they do not degrade the attenuation of the temperature fluctuations. To do so, we employ Eq. (14). Figure 5 (top) shows the attenuation at the radiative cut-off angular frequency—cf. Eq. (18), for two materials as a function of the length of the supports ℓ and the total cross section A_s of the supports. For the calculations, the layer thickness has been set to $h=0.5$ mm and as material we chose aluminum. The distance between the layers ℓ is kept such that $r_{i+1}/r_i = 0.9$ (the distance between the layers is $0.1r_i$). The total cross-section of the supports has been constraint to $A_j/10$ (the supports only cover 10% of the thermal shields area). For larger areas the model is not accurate since β is no longer of the form given in Eq. (16)—see Sec. 4. However, such large areas for the supports are unusual for typical designs of thermal shields. The properties of the support materials are given in Table 1. The materials are chosen due to their low thermal conductivity.

Figure 5 shows how the behavior of the system changes at a certain length ℓ_{\min} : For fixed $\ell (> \ell_{\min})$, increasing the cross-section of the supports improves the attenuation of temperature fluctuations and for $\ell < \ell_{\min}$ diminishes it. This turning point, ℓ_{\min} , occurs for $\tau_s \gtrsim 2\tau$, where

$$\tau_s \simeq \frac{\ell^2 \rho_s c_s}{\kappa_s} \quad (24)$$

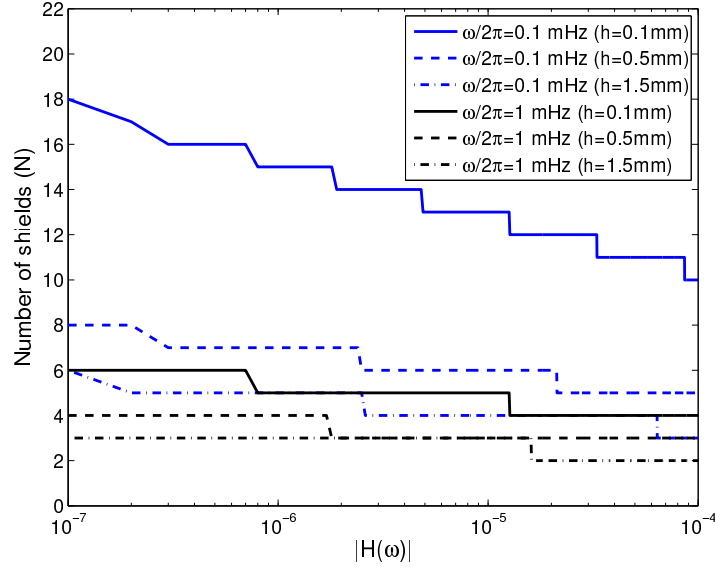


Fig. 4. Number of shields needed as a function of the required attenuation for 0.1 mHz and 1 mHz and different shield thickness, h .

Table 1. Properties of the support materials used for the numerical evaluation in Fig. 5.

Material	κ_s [$\text{W m}^{-1} \text{K}^{-1}$]	ρ_s [kg m^{-3}]	c_s [$\text{J kg}^{-1} \text{K}^{-1}$]
Ultem 1000	0.122	1280	2000
Macor	1.46	2520	790

and $\tau = \theta C$. Therefore, the respective minimum length of the supports is:

$$\ell_{\min} \simeq \left(\frac{\rho c h}{\varepsilon \sigma T_0^3} \frac{\kappa_s}{c_s \rho_s} \right)^{1/2}, \quad (25)$$

which depends only on the materials of the shields and supports as well as the thickness of the layers h . For instance, for $h=0.5$ mm we have $\ell_{\min} = 35.5$ mm for Ultem 1000 and $\ell_{\min} = 150$ mm for Macor. It is important to remark that once $\ell > \ell_{\min}$ the support cross-sections do not have any constraints provided $A_s/A_j < 1/10$, which we assumed in the derivation. Note that it is not necessary that the shield layers are at that distance ℓ_{\min} , because the thermal supports can be routed conveniently between the shields allowing still a compact designs as long as the radiative heat transport between the supports and the layers is negligible. The latter assumption of our model can be met by using supports with high reflectivity coatings. This at first glance counter-intuitive change in behavior occurs since for a certain length increasing the area of the support causes an increase of the thermal capacitance, which compensates the reduction of the thermal resistance due to the larger cross-section of the support.

The bottom left plot in Fig. 5 shows the attenuation at the radiative cut-off angular frequency ω_c for a given A_s as a function of the length of the supports for Ultem 1000 and Macor. The minimum length corresponds to that where the attenuation is $1/\sqrt{2}$, i.e., the length where the cut-off angular frequency of the thermal shield with supports does not change with respect to the one without supports. The minimum length for Ultem is much shorter than the one for

Macor and also the attenuation drops much faster when increasing the length. However, in the asymptotic limit the attenuation for Macor is stronger than the Ultem one:

$$\lim_{\ell \rightarrow \infty} H(\omega_c) = \frac{1}{1 + i + \left(\frac{i}{\omega_c} \rho_s c_s \kappa_s\right)^{1/2} \frac{1}{C_j} A_s}. \quad (26)$$

The right bottom plot shows the transfer function for three scenarios: (i) $\ell = \ell_{\min}/2$, (ii) $\ell = 2\ell_{\min}$ and (iii) radiation only. The rest of the parameters are kept the same. The change of behavior in the attenuation is again clear. It is also interesting that combining the thermal shields and the supports (radiation and conduction) adequately a dip in the transfer function can be obtained. Such behavior could be used to design thermal shields, where temperature fluctuations have to be attenuated in a very narrow frequency band.

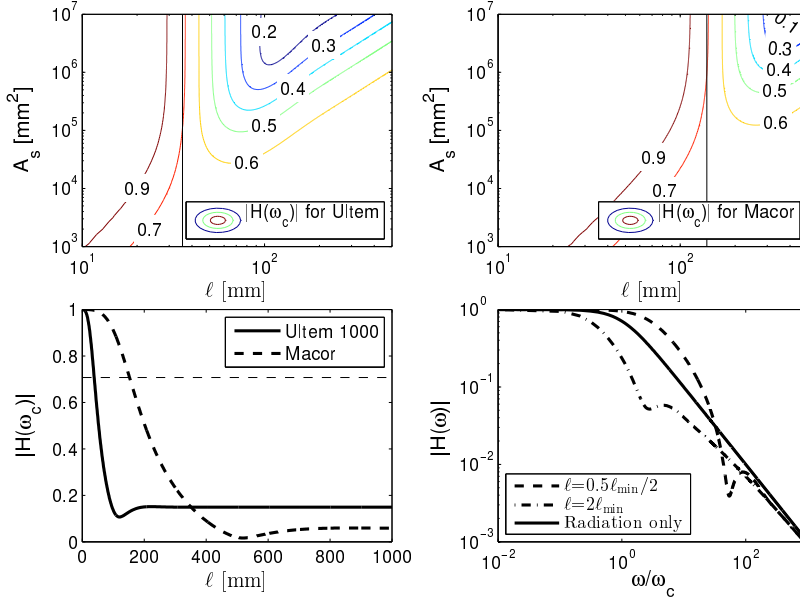


Fig. 5. Transfer function for different support lengths and cross-sections for two materials and $h=0.5$ mm. Top left: Ultem 1000. Top right: Macor. The vertical dashed lines indicate ℓ_{\min} . Bottom left: the attenuation of temperature fluctuations at ω_c for different support lengths. We set in this calculations $r_{i+1}/r_i = 0.9$ and $A_s/A_j = 0.1$. If $\ell < \ell_{\min}$ the attenuation is degraded around ω_c compared to a system without the supports (the attenuation at ω_c is $1/\sqrt{2}$ —horizontal dashed line). Once $\ell > \ell_{\min}$, increasing the length of the supports improves the damping of temperature fluctuations. This improvement reaches an asymptotic value not too far from ℓ_{\min} . Bottom right: transfer functions as a function of the frequency for two scenarios with different support lengths and the radiative case only.

The results shown in Fig. 5 are for one thermal shield consisting of two layers. When nesting N shields the transfer function including the supports can be approximated by:

$$\tilde{H}(\omega) \simeq \left[\frac{\sinh \ell q_s + q_s \theta \kappa_s A_s}{(1 + i\tau\omega) \sinh \ell q_s + q_s \theta \kappa_s A_s \cosh \ell q_s} \right]^N. \quad (27)$$

This assumption of uncoupled layers yields errors similar to those shown in Fig. 1. The derivation of the solution for the coupled case is given in Appendix B.

4. Analytical solutions and FEM simulations results

In this section, we compare the results and properties found in the previous section with the results of FEM simulations performed with commercial software (Comsol). Figure 6 shows the transfer function, if we take only radiation into account. The model considered here consists of four aluminum layers ($N=3$) with $\varepsilon=0.03$ and $h=1.5$ mm. The radii of the shields are from the inner shield to the outer: 100 mm, 111.1 mm, 123.9 mm and 137.9 mm, respectively i.e., the ratio r_{i+1}/r_i has been kept at approximately 0.9. The maximum mesh element size is 31 mm and the minimum one is 5.5 mm. The mesh settings are valid for the rest of the simulations with finer mesh when including the conductive thermal links. We use a sweep sine with frequencies from $1 \mu\text{Hz}$ to $50 \mu\text{Hz}$ as the boundary condition of the outermost layer of the thermal shield. The transfer function is calculated as the ratio of the Fourier transformed temperature at the innermost and the outermost layer of thermal shield. Figure 6 shows that the numerical simulations are in very good agreement with the analytical results calculated using Eq. (9). The discrepancy between the simulations and the model is close to the expected one due to the fact of assuming $\tau_i = \tau_{i+1}$ when $r_{i+1}/r_i=0.9$ —see Fig. 2 and Fig. 3.

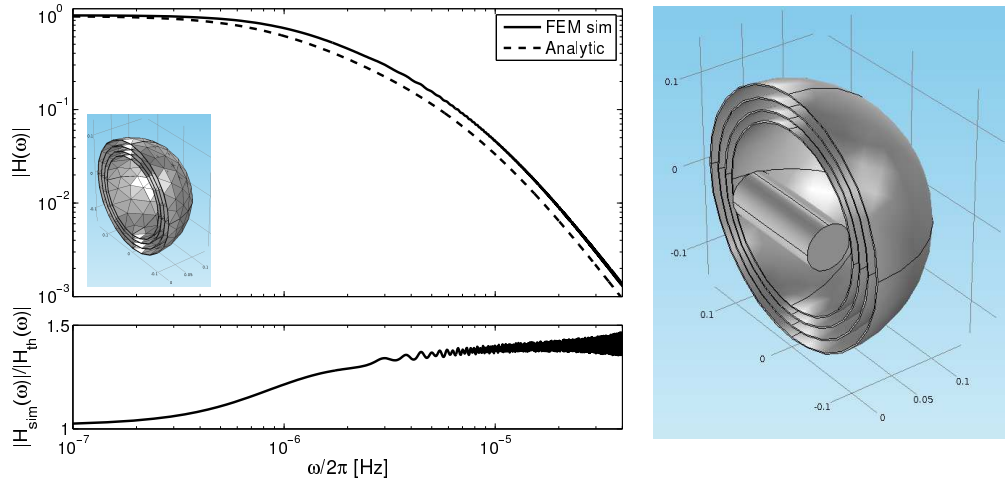


Fig. 6. Left: FEM simulation and theoretical results —cf. Eq. (9) for the transfer function of a thermal shield consisting of four aluminum layers ($N=3$) considering only radiation. The bottom panel shows the ratio between the results. Right: thermal shield model used for the calculations and simulations. The OR (12.5 cm) is not included in the simulations. The mesh is shown in the left figure inset.

Figure 7 (left panel) shows the simulations performed to evaluate the behavior found in Sec. 3.2, when conductive elements are included in the model. Different configurations have been simulated with supports (70 mm in length) used to connect the thermal shield layers. The properties of the shields and the supports have been tweaked to achieve different ℓ_{\min} values. The simulations were carried out for different cross-sections with an oscillating temperature at $\sim \omega_c$ as the boundary condition in the outer aluminum layer. Three configurations have been simulated for a given $\ell=70$ mm and different ℓ_{\min} : (i) $\ell_{\min} = 1.75\ell=40$ mm (blue trace), (ii) $\ell_{\min} = 0.58\ell=120$ mm (red trace) and (iii) $\ell_{\min} = 0.2\ell = 350$ mm. The results from the simulations (“x” marks) and from the analytical equations (dashed lines) are also in good agreement. The right panel in Fig. 7 shows the simulated and analytical transfer functions for different parameters, when the supports are included. The model considers only one shield and

the properties have been chosen to simulate different expected behaviors. They are summarized in Table 2. Cubes have been used instead of spheres and, therefore, A_j needs to be calculated accordingly since it appears in θ in Eq. (14). The results from the simulations and the analytical calculations are in very well agreement, too.

Table 2. Properties of the supports used in Fig. 7 (right panel): $\rho_s=1200 \text{ kg m}^3$, $c_s=7200 \text{ J kg}^{-1} \text{ K}^{-1}$, $\ell = 0.053 \text{ m}$; properties of the layers of the thermal shield: aluminum with $h=1.5 \text{ mm}$, $\varepsilon=0.03$, $A_2=0.06 \text{ m}^2$, $r_2=0.1 \text{ m}$ and $r_1=0.153 \text{ m}$ ($2r$ is the length of cube's edge).

Model	$\kappa_s [\text{W (m K)}^{-1}]$	$A_s [\text{m}^2]$
(i)	0.122	10^{-3}
(ii)	0.122	6.2×10^{-3}
(iii)	12.2	10^{-3}
(iv)	12.2	6.2×10^{-3}

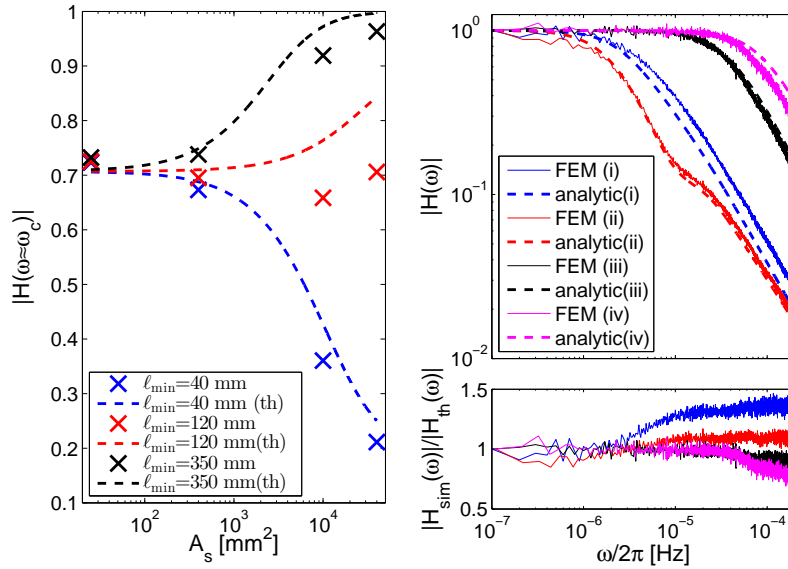


Fig. 7. FEM simulations and analytical results. Left: temperature fluctuations attenuation at ω_c for $\ell > \ell_{\min}$ (blue) and $\ell < \ell_{\min}$ (red and black). $\ell=70 \text{ mm}$ for all the simulations. Right: transfer functions for different models —see Table 2, and the ratios between the simulations and the analytical transfer functions, which indicate the good agreement between them. The simulations failed for frequencies higher than $100 \mu\text{Hz}$ due to numerical resolution issues.

Finally, simulations have been performed to quantify two limitations of the analytical model and its assumptions: (i) the ratio of the cross-section of the supports and the area of the shields was assumed to be sufficiently small —see Sec. 3.2 and, (ii) radiative heat transfer between the supports and the shields was neglected. If (i) is not met, the view factors used for the derivation in Sec.3.2 are not valid anymore. Figure 8 (left) shows the comparison between the simulations (solid lines) and the model (dashed lines). The results are in good agreement for ratios smaller than ~ 0.15 . The discrepancy at the dip for $A_s/A_j = 0.15$ is mainly due to the limited frequency resolution of the estimated transfer function from the simulations. For larger

ratios (black trace), the errors become significant. For instance, for $A_s/A_j = 0.66$ the theoretical transfer function and the one obtained by FEM simulations differ by a factor of ~ 10 at high frequencies. However, such large ratios are rarely used in thermal shield designs. The right panel in Fig. 8 compares the simulations when including radiative heat transfer between the supports and the shield layers. The simulations (solid and dashed lines) and the model (dash-dotted lines) are in well agreement for small ϵ_s .

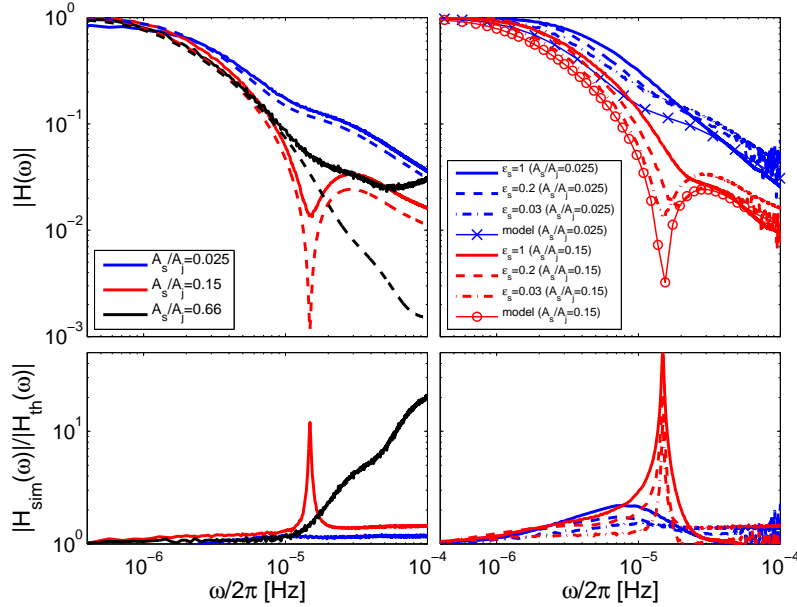


Fig. 8. Left: FEM simulations (solid lines) and theoretical transfer functions (dashed lines) for different values of the supports cross sections and no radiation between the supports and the shields, $\epsilon_s=0$. The model agrees with the simulations when the total area of the supports is significantly smaller than the area of the shield ($A_s/A_j \lesssim 0.15$) as previously stated. The bottom plot shows the ratio between the simulations and the analytical transfer functions. The discrepancies are significant for $A_s/A_j=0.66$ at high frequencies. Right: FEM simulations (solid and dashed lines) for different supports emissivities and A_s/A_j ratios and the theoretical transfer functions (dash-dotted lines) where $\epsilon_s = 0$. The difference between the simulations and the model appears for large emissivity values. The bottom plot shows the ratios between the numerical simulations transfer functions and the analytical model.

5. Conclusion

Highly sensitive interferometers and experiments testing fundamental physics require an isolation against external and environmental influences. In particular, the attenuation of external temperature fluctuations by several orders of magnitude at low frequencies (sub-milli-Hertz and milli-Hertz) using thermal shields is crucial. Such thermal shields are typically designed by numerical FEM simulations, which are time consuming and precision limited. Otherwise, simple analytical “toy” models that do not reflect all the features of the system are employed. However, an accurate analytical method is to our knowledge still lacking. We derived in this paper a fast and accurate method to calculate the performance of thermal shields in the frequency domain. This analysis has also yielded interesting results, such as that for some configurations a dip in

the transfer function can be achieved in a narrow frequency range, and that the cross-section of the supports can be increased without jeopardizing the shields performance as far as they reach a critical minimum length. The former property is of interest for experiments with a narrow and well-known frequency range, such as BOOST. The latter can be useful for space experiments to design mechanically stable shields without losing thermal insulating capability. The analytical model has been validated by comparing it with the results obtained by FEM simulations. This method allows for quick investigations of the design of thermal shields to optimize its performance, which later can be assessed and fine-tuned by FEM simulations.

Appendix A: Derivation of the transfer function considering only radiation

In this appendix, we derive the transfer function considering only radiation. The electrical circuit equivalent to N thermal shields and the optical resonator is shown in Fig. 9 —see Sec. 2.1 for the definitions of θ_{ij} and C_i . Note that this analogy is only valid as far as the linearization used in Eq. 4 of the radiative thermal heat transfer holds.

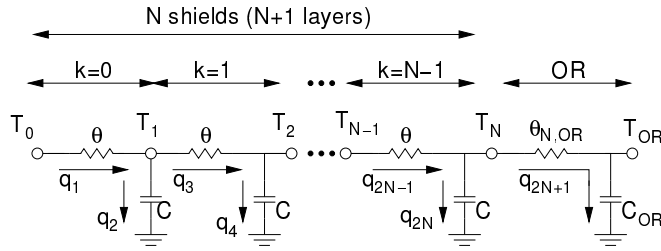


Fig. 9. Electrical circuit equivalent to a thermal shield consisting of N shields including the optical resonator. The thermal resistance and heat capacitance are assumed to be the same for all of the layers except the resonator one.

The transfer function is defined as the ratio between the first and the last temperature node, i.e., $\tilde{T}_{OR}/\tilde{T}_0$, where *tildes* ($\tilde{}$) stand for Fourier transforms. The transfer function is found by solving the following system of equations, which is constructed by applying the Kirchoff's circuit laws.

$$\tilde{T}_k - \tilde{T}_{k+1} - \theta q_{2k+1} = 0, \quad k = 0 \dots N-1 \quad (\text{A1})$$

$$\tilde{T}_{k+1} - \frac{1}{sC} q_{2k+2} = 0, \quad k = 0 \dots N-1 \quad (\text{A2})$$

$$q_{2k+1} - q_{2k+2} - q_{2k+3} = 0, \quad k = 0 \dots N-1 \quad (\text{A3})$$

$$\tilde{T}_N - \tilde{T}_{OR} - \theta_{OR} q_{2N+1} = 0 \quad (\text{A4})$$

$$\tilde{T}_{OR} - \frac{1}{sC_{OR}} q_{2N+1} = 0, \quad (\text{A5})$$

where q is the heat flow (the current in the analogy of electrical circuits) from one node to the other in units of Watt and the temperature (the voltage in the analogy), and $s = i\omega$ is the Laplace variable with the Fourier frequency ω . All the thermal resistances and capacitances are assumed to be equal (except the optical resonator's one). The solution of this system of equations can be written in a compact form using the Pascal triangle numbers. If one does not consider the optical resonator the transfer function is the one given by Eq. (9). The one including the resonator is given by Eq. (11).

Appendix B: Derivation of the transfer function including conductive links

As stated in Sec. 2.2 the lumped model is not adequate to represent the conductive heat transfer via the supports connecting the shields. Consequently, the Fourier heat equation has to be used. Radiative heat transfer is not considered between the supports and the thermal shields, i.e., the supports are assumed to be coated with materials with very low emissivity or, alternatively they have small areas of sight. In this scenario, the conductive heat transfer within the supports occurs only in one direction —see Fig. 10:

$$\rho_s c_s \frac{\partial T(x,t)}{\partial t} = \kappa_s \frac{\partial^2 T(x,t)}{\partial x^2}, \quad -\ell \leq x \leq 0, \quad (\text{B1})$$

where ρ_s , c_s and κ_s are the density, the specific heat and the thermal conductivity of the supports. The transfer function is found by applying the Fourier transform to Eq. (B1) [29]:

$$\frac{d^2 \tilde{T}(x)}{dx^2} - q_s^2 \tilde{T}(x) = 0, \quad (\text{B2})$$

where $q_s = \left(i \frac{\rho_s c_s}{\kappa_s} \omega\right)^{1/2}$. Equation (B2) is solved with the following boundary conditions (known boundary temperature at the outer most layer, \tilde{T}_0 , and continuous heat flux at the interface):

$$\tilde{T}(-\ell) = \tilde{T}_0 \quad (\text{B3})$$

$$-\kappa_s A_s \left. \frac{d\tilde{T}(x)}{dx} \right|_0 = i\omega C \tilde{T}(0) + \frac{\tilde{T}(0) - \tilde{T}(-\ell)}{\theta}, \quad (\text{B4})$$

The transfer function is $\tilde{T}(0)/\tilde{T}_0$ and the solution is given in Eq. (14).

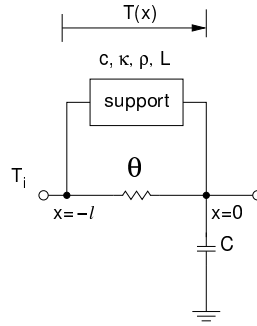


Fig. 10. Model including the conductive link in a thermal shield layer. Typically, the support cannot be modeled as a thermal resistance since large thermal gradients are present along it. Instead the Fourier heat transfer equation needs to be solved. The model does not include radiative heat transfer from the supports to the shields.

The exact solution for N shields plus the resonator and the supports is found by solving the following system of differential equations —see Fig. 11:

$$\frac{d^2 \tilde{T}_k(x)}{dx^2} - q_s^2 \tilde{T}_k(x) = 0, \quad -(N - (k - 1))\ell \leq x \leq -(N - k)\ell \quad (\text{B5})$$

with $k = 0 \dots N$. The boundary conditions are that the temperature and the heat flux are continuous across the interfaces:

$$\tilde{T}_0(-(N+1)\ell) = \tilde{T}_0 \quad (\text{B6})$$

$$\tilde{T}_k(-(N-k)\ell) = \tilde{T}_{k+1}(-(N-k)\ell) \quad (\text{B7})$$

$$-\kappa_s A_s \left. \frac{d\tilde{T}_k(x)}{dx} \right|_{-(N-k)\ell} = i\omega C \tilde{T}_k(-(N-k)\ell) + \frac{\tilde{T}_k(-(N-k)\ell) - \tilde{T}_k(-(N-k+1)\ell)}{\theta} \quad (\text{B8})$$

$$-\kappa_s A_s \left. \frac{d\tilde{T}_N(x)}{dx} \right|_0 = i\omega C_{\text{OR}} \tilde{T}_N(0) + \frac{\tilde{T}_N(0) - \tilde{T}_N(-\ell)}{\theta_{\text{OR}}}, \quad (\text{B9})$$

where here $k = 0 \dots N - 1$.

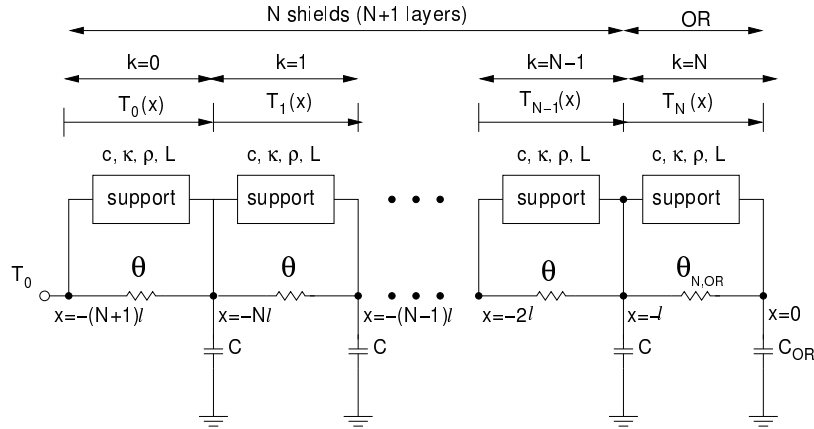


Fig. 11. Model including the conductive link and the optical resonator for N thermal shields and the OR.

Acknowledgments

The authors appreciate valuable discussions with Alexander Milke, Thilo Schuldts and Martin Siemer. This work was supported by the German space agency (Deutsches Zentrum für Luft- und Raumfahrt DLR) with funds provided by the Federal Ministry of Economics and Technology under grant numbers 50 QT 1401 and the DFG Sonderforschungsbereich (SFB) 1128 Relativistic Geodesy and Gravimetry with Quantum Sensors (geo-Q).